The influence of the Jahn-Teller-effect at Fe^{2+} on the structure of chromite at high pressure

Atsushi Kyono,[ab*] Stephen A. Gramsch,[b] Takamitsu Yamanaka,[b] Daijo Ikuta,[c] Muhtar Ahart,[b]

Bjørn O. Mysen,[b] Ho-kwang Mao,[b] and Russell J. Hemley[b]

[a]Division of Earth Evolution Sciences, Graduate School of Life and Environmental Sciences,

University of Tsukuba, 1-1-1 Tennodai, Tsukuba, Ibaraki 305-8572, Japan

[b]Geophysical Laboratory, Carnegie Institution of Washington, 5251 Broad Branch Road, N.W.,

Washington D.C. 20015-1305, USA

[c]HPCAT, Geophysical Laboratory, Carnegie Institution of Washington, 9700 South Cass Ave., Bldg. 434E,

Argonne, Illinois, 60439, USA

Correspondence author: A. Kyono

Address: Division of Earth Evolution Sciences, Graduate School of Life and Environmental Sciences,

University of Tsukuba, 1-1-1 Tennodai, Tsukuba, Ibaraki 305-8572, Japan

Correspondence e-mail: kyono@geol.tsukuba.ac.jp

Phone: +81-29-853-7176,   Fax: +81-29-853-7887

ABSTRACT

The crystal structure of chromite $FeCr_2O_4$ was investigated to 13.7 GPa and ambient temperature with single-crystal x-ray diffraction techniques. The unit-cell parameter decreases continuously from 8.3832 (5) Å to 8.2398 (11) Å up to 11.8 GPa. A fit to the Birch-Murnaghan equation of state (EoS) based on the P-V data gives: $K_0 = 209$ (13) GPa, $K' = 4.0$ (fixed), and $V_0 = 588$ (1) $Å^3$. The FeO_4 tetrahedra and CrO_6 octahedra are compressed isotropically with pressure with their Fe-O and Cr-O bond distances decreasing from 1.996 (6) to 1.949 (7) Å and from 1.997 (3) to 1.969 (7) Å, respectively. The tetrahedral site occupied by the Fe^{2+} cation is more compressible than the octahedral site occupied by the Cr^{3+} cation. The resulting EoS parameters for the tetrahedral and the octahedral sites are $K_0 = 147$ (9) GPa, $K' = 4.0$ (fixed), $V_0 = 4.07$ (1) $Å^3$ and $K_0 = 275$ (24) GPa, $K' = 4.0$ (fixed), $V_0 = 10.42$ (2) $Å^3$, respectively. A discontinuous volume change is observed between 11.8 GPa and 12.6 GPa. This change indicates a phase transition from a cubic (space group *Fd-3m*) to a tetragonal structure (space group *I4$_1$/amd*). At the phase transition boundary, the two Cr-O bonds parallel to the *c*-axis shorten from 1.969 (7) Å to 1.922 (17) Å and the other four Cr-O bonds parallel to the *ab* plane elongate from 1.969 (7) Å to 1.987 (9) Å. This anisotropic deformation of the octahedra leads to tetragonal compression of the unit cell along the *c*-axis. The angular distortion in the octahedron decreases continuously up to 13.7 GPa, whereas the distortion in the tetrahedron rises dramatically after the phase transition. At the pressure of the phase transition, the tetrahedral bond angles along the c-axis direction of the unit cell begin decreasing from 109.5° to 106.6 (7)°, which generates a "stretched" tetrahedral geometry. It is proposed that the Jahn-Teller effect at the

tetrahedrally-coordinated Fe^{2+} cation becomes active with compression and gives rise to the tetrahedral angular distortion, which in turn induces the cubic-to-tetragonal transition. A qualitative molecular orbital model is proposed to explain the origin and nature of the Jahn-Teller effect observed in this structure and its role in the pressure-induced phase transition.

Introduction

Chromite, with the ideal chemical composition $FeCr_2O_4$, belongs to the group of normal spinels, which are present as accessory minerals in the Earth's crust and mantle over a wide range of pressures and temperatures. Because of their importance to the physical properties, dynamics, and differentiation of the Earth's interior, the spinel group minerals have long been of central interest in studies of the deep Earth (e.g., Peltier and Solheim 1992, Shim et al. 2001, Katsura et al. 2003). The spinel group minerals are classified into three series (Deer et al., 1966) according to the dominant trivalent ion; the spinel series (Al^{3+}-dominant), the magnetite series (Fe^{3+}-rich) and the chromite series (Cr^{3+}-rich), with significant solid solution occurring within and between the three spinel series. The spinels also exhibit rich high-pressure and -temperature behavior. The $MgAl_2O_4$ spinel decomposes at 15-16 GPa and 1200-1600 °C to a mixture of MgO periclase and Al_2O_3 corundum, which recombine into $MgAl_2O_4$ with the $CaFe_2O_4$-type structure at 25-27 GPa and 1400-2000 °C (Akaogi et al. 1999; Enomoto et al. 2009). Magnetite (Fe_3O_4) transforms into a high-pressure modification (h-Fe_3O_4) with the $CaMn_2O_4$-type (and $CaTi_2O_4$-type) structure at 24 GPa and 550 °C, which persists up to at least 43 GPa (Fei et al. 1999; Haavik et al. 2000).

A high-pressure polymorph of chromite has been discovered in the shock-metamorphosed Suizhou meteorite as the mineral xieite (Chen et al. 2003a,b). This polymorph is described as having the orthorhombic $CaTi_2O_4$-type structure, with estimated P-T conditions for the phase transition from chromite to the $CaTi_2O_4$-type polymorph at 20-23 GPa and 1800 to 2000 °C. On the other hand, no phase

change has been observed up to 26.8 GPa and 355 °C with a natural chromite as the starting material (Fan

et al. 2008). A preliminary experiment (Shu et al. 2007) showed that a pressure-induced phase transition

in the natural chromite occurs at 29 GPa at room temperature, but these experimental data were too

limited to establish the mechanism of the phase transition between chromite and the high-pressure

polymorph. Moreover, the natural chromite employed in these studies (Chen et al. 2003b; Shu et al. 2007;

Fan et al. 2008) includes not only Fe and Cr, but also a large amount of metal substitution, including Mg,

Mn, Al, V, Na, and Ti.

Because the physical properties of the spinels are significantly controlled by their chemical

compositions, the P-T conditions for the phase transition in chromite are expected to be sensitive to

composition and therefore should be examined using a pure chromite with the ideal composition. Until

now, however, no high pressure experiments have been conducted on a chromite with the ideal chemical

composition. In pure chromite, tetrahedral sites are fully occupied by Fe^{2+} cations, which exhibit the

Jahn-Teller effect at low temperature Goodenough (1964).   Recently, the importance of the Jahn-Teller

effect in understanding the structural phase transitions in $FeCr_2O_4$ has been noted (Arima et al. 2007;

Ohgushi et al. 2008; Tomiyasu et al. 2008; Bordács et al. 2009; Ohtani et al. 2010), and a systematic

change in the crystal structure with temperature and composition has been documented. Yamanaka et al

(2009) have also investigated a structural phase transition in ulvöspinel $FeTi_2O_4$, apparently due to the

Jahn-Teller effect at the tetrahedrally-coordinated Fe^{2+} cation.

In this study, we have investigated the pressure-induced phase transition of a chromite sample with

the ideal end-member composition. We report results of high pressure single-crystal x-ray diffraction studies up to 13.7 GPa, and discuss the influence of the Jahn-Teller effect at the Fe^{2+} cation on structural transitions in chromite under high pressure.

Experimental Procedure

Pure chromite powder was synthesized from a mixture of Fe_2O_3 and Cr_2O_3, which was heated at 1400 °C for 48 hours in a controlled CO/CO_2 gas flow ($\log f_{O2} = -8.0$). Single crystals were grown from the pure chromite powder using the sublimation method at 1300 °C. Crystals with well-developed faces, sharp edges, and euhedral form with size up to 300 μm were obtained. For x-ray powder diffraction analysis, these single crystals were ground to a fine powder with an agate mortar and pestle. X-ray powder diffraction data were collected with a Rigaku R-AXIS RAPID diffractometer using Mo$K\alpha$ radiation (λ = 0.70930 Å). No impurities were detected in the x-ray patterns. Measured Bragg peak positions were determined using the profile fitting routine in JADE 9.0 (Materials Data Inc., Livermore, CA USA). Furthermore, a preliminary x-ray diffraction study of the crystalline material under high pressure has been performed in a diamond anvil cell (DAC) using synchrotron radiation at beamline 16-BM-D (HPCAT) at the Advanced Photon Source (APS), Argonne National Laboratory. The sample powder was loaded with several ruby spheres (a pressure marker) into a 150 μm hole drilled in a tungsten gasket and compressed in a neon pressure medium up to 17.9 GPa. The wavelength of the monochromatic incident beam was 0.42620 Å. The beam was focused using a pair of Kirkpatrick-Baez mirrors to a focal

spot of approximately 5 by 15 μm^2. A two-dimensional imaging plate detector (MAR345 image plate device) was placed approximately 460 mm from the sample. The powder x-ray diffraction patterns are shown in Figure 1. The powder diffraction pattern collected at 17.9 GPa was analyzed by the Rietveld method with the RIETAN-2000 program (Izumi and Ikeda, 2000). The result of the pattern fitting and structure refinement by Rietveld analysis is presented in Figure 2.

A single crystal with dimensions $100 \times 100 \times 80$ μm was used for the single-crystal x-ray diffraction experiment. Measurements at ambient pressure and temperature conditions were carried out with a Huber four-circle diffractometer using an 18 kW rotating Mo-anode x-ray generator at 50 kV and 240 mA with a scintillation point detector. The incident x-ray wavelength of 0.71069 Å was produced by a Si (111) single-crystal monochromator and 0.8 mm double pinhole collimator. The 2θ range for diffraction was from 8° to 60°. The 8-position centering method (King and Finger 1979) was applied to a set of observed diffraction maxima for unit cell parameter determination. An x-ray intensity data collection was carried out in ω-scan mode, with a scan speed of 1.5 °/min, scan width of 1.0° in ω, and step interval of 0.025°/step. A total of 264 reflections were observed and 58 crystallographically independent reflections with $F_o > 4\sigma(F_o)$, the intensity threshold for accepting a reflection as strong, were used for least-squares refinement. Intensities were corrected for Lorentz and polarization effects. An absorption correction was performed with the program ABSORB (Angel 2004). Refinements of atomic positions and anisotropic displacement parameters were carried out using SHELXL-97 (Sheldrick 1997). From estimated crystal field stabilization energies (CFSE), Cr shows the strongest preference for

octahedral coordination among transition metal cations (Dunitz and Orgel, 1960). Although the possibility that Fe^{2+} cations occupy the octahedral site in chromite has been investigated by Mössbauer and IR spectroscopy, these spectra (Lenaz et al 2004) indicate that the octahedral site is almost exclusively occupied by Cr^{3+}. Therefore, the least-squares refinement was carried out assuming a completely ordered structure, which has the tetrahedral site fully occupied by Fe^{2+} and the octahedral site fully occupied by Cr^{3+}. The structure refinement using the intensity data at ambient conditions converged to $R_{int} = 0.0551$, $R_1 = 0.0344$ and $wR_2 = 0.0642$ for 58 unique reflections. Details of the data collection, structure refinements, and crystal structures are collected in Table 1.

After data collection under ambient conditions, the crystal was mounted in epoxy and polished for high pressure x-ray diffraction experiments that were carried out at beamline 16-BM-D at the APS. The sample was polished to 20 μm thickness and a small crystal fragment with dimensions of about $50 \times 40 \times 20$ μm was mounted in a symmetric diamond anvil cell with 300 μm culets using a tungsten gasket with a 120 μm diameter hole as the sample chamber. One diamond anvil was supported by a cubic boron nitride (c-BN) backing plate, and the other anvil by a tungsten carbide (WC) backing plate. Pressures inside the DAC were measured with the ruby luminescence method (Mao et al. 1986). The DAC was loaded with neon as the pressure medium, and mounted on a motor driven stage with the WC seat on the downstream side, and the c-BN seat on the upstream side. The wavelength of the monochromatic incident x-ray beam was 0.41340 Å. This beam was focused to a focal spot of 5 by 15 μm^2 by using a pair of Kirkpatrick-Baez mirrors. The MAR345 image plate detector was placed approximately 317 mm from the sample.

Diffraction intensities were measured using a continuous ω-oscillation scan mode over the range from

-30° to +30° with an exposure time of 20 seconds per degree of oscillation. The intensities were corrected

for Lorentz and polarization effects, but absorption effects were neglected in view of the small crystal size.

A total of 8 high pressure data collections (P = 3.8, 8.1, 9.5, 10.8, 11.8, 12.6, 13.7, and 15.0 GPa) were

carried out. At a pressure of 15.0 GPa, however, the refinement failed to converge to a satisfactory level

because some diffuse spots appeared in the diffraction pattern.

The data were processed using FIT2D software (Hammersley, 1998). Reduction of the

three-dimensional distribution of x-ray diffraction maxima in reciprocal space and diffraction intensities

were performed using standard beamline codes (Dera, 2007). The d-spacing values for the sample were

corrected by diamond diffraction, which served as an internal standard by application of the diamond

equation of state (Gillet at al. 1999). The deviations between observed and calculated d-spacing values

from the diamond EoS are normally less than 0.01 Å. Unit-cell parameters were determined with a

non-linear least-squares fitting program (Holland and Redfern 1997). The structure was then refined using

SHELXL-97 (Sheldrick 1997). All atomic positions were refined with isotropic thermal parameters.

Details of crystal structure refinements are listed in Table 1. The structural variations determined by the

single-crystal X-ray diffraction measurements are shown in Figure 3.

Results and Discussion

Equation of state and phase transitions

Figure 1 shows the high pressure powder x-ray diffraction patterns for chromite. Some extra peaks were clearly present above 16.1 GPa, and a slight asymmetry of the (311) and (220) peaks can be observed at 13.9 GPa. These features are indicative of a phase transition in chromite. Fan et al. (2008) investigated the thermal equation of state of a natural chromium spinel up to 27 GPa and 355 K, but reported no phase transition in this pressure range. Shu et al. (2007) reported a phase transition at 29 GPa at room temperature. In the present study, the x-ray diffraction measurements are carried out using a pure chromite sample with end-member composition of $FeCr_2O_4$. Therefore, the difference in the phase transition pressures can be ascribed to compositional differences between samples and the resulting chemical disordering and intracrystalline cation exchange between tetrahedral and octahedral sites.

The diffraction pattern measured at 17.9 GPa was selected for Rietveld analysis of the high-pressure polymorph, because several diffraction lines are clearly different from those of cubic spinel. Figure 2 shows the result of this analysis. The diffraction features perfectly match those of a phase with tetragonal symmetry [$R_B = 0.0211$, $R_F = 0.0137$, $S = 1.35$] in space group $I4_1/amd$ and with unit-cell parameters $a = 5.87$ (7) Å, $c = 7.91$ (8) Å (Fig. 2). A phase with a crystal structure corresponding to space group $I4_1/amd$ has been observed at low temperature as well (Tsukuda et al. 2010).

Single-crystal x-ray measurements at ambient pressure were initially carried out on three different single crystals to confirm the homogeneity of the chromite sample. Differences in the a unit-cell parameter between the individual samples were below 0.002 Å, suggesting that the specimens are homogeneous and with no significant differences in crystallinity. Unit cell parameters determined by

least-squares refinement using 15-20 reflections are reported in Table 2. Figure 3 (a) shows the variation

in unit cell volume of the $FeCr_2O_4$ structure with pressure. The cell volume of the chromite spinel phase

decreases smoothly with pressure up to 11.8 GPa. The pressure-volume data were fitted using a

Birch-Murnaghan equation of state as implemented in EOSFIT 5.2 (Angel 2002). The EoS parameters are

given in Table 2. Regardless of the fact that naturally occurring chromite has Na, Mg, Fe^{2+} and Ti in the

tetrahedral site and Cr^{3+} and Al in the octahedral site, the bulk modulus [K_0 = 209 (9) GPa, Fan et al.

2000] is quite close to that of the ideal chemical composition $FeCr_2O_4$ determined in the present work.

For comparison, the bulk modulus for franklinite $ZnFe_2O_4$ with octahedral Fe^{3+} and magnesioferrite

$MgFe_2O_4$ with tetrahedral Fe^{3+} are 166 (3) GPa (K' = 9.3, Levy et al. 2000) and 182 (1) GPa (K' = 6.3,

Levy et al. 2004), respectively. For magnetite Fe_3O_4 with tetrahedral Fe^{3+} and octahedral Fe^{2+} and Fe^{3+}, K_0

= 182 (4) GPa (K' = 3.6, Gotta et al. 2007) and 186 (5) GPa (K' = 4.0, Finger et al. 1986). Ulvöspinel

Fe_2TiO_4 with tetrahedral Fe^{2+} has K_0 = 185 (20) GPa (K' = 4.0, Yamanaka et al. 2009). K_0 values for the

chromium spinels $MgCr_2O_4$, $MnCr_2O_4$, and $ZnCr_2O_4$ with octahedral Cr^{3+}, obtained by Hartree-Fock

calculations, are 197.3 GPa (K' = 3.94), 205.8 GPa (K' = 3.67), ad 215.0 GPa (K' = 3.96), respectively

(Catti et al. 1999). The bulk modulus for chromite is therefore similar to the theoretical prediction for the

chromium spinels, but it is slightly larger than that of other spinels with tetrahedral Fe^{2+}.

A discontinuous change in the volume of $FeCr_2O_4$ is observed between 11.8 GPa and 12.6 GPa (Fig.

3 (a)). Therefore, Miller indices for the cubic structure are reassigned to those corresponding to a

tetragonal structure through the transformation matrix (1/2, -1/2, 0) (1/2, 1/2, 0) (0, 0, 1). The resulting

unit cell parameters are $a = 5.813$ (1), $c = 8.214$ (8) Å and V = 275.6 (2) Å^3, which is nearly equal to half

the volume of the cubic lattice, as predicted for a transformation from a face-centered cubic structure in

space group Fd-$3m$ to a body-centered tetragonal structure in space group $I4_1/amd$. To model the

compressibility of the unit cell better, the volume of the tetragonal lattice is doubled in Figure 3 (a). The

variation in unit-cell parameters as a function of pressure is shown in Figure 3 (b). The a unit-cell

parameter in the tetragonal lattice is therefore multiplied by $2^{1/2}$ in the figure. The pseudocubic a unit-cell

parameter in the tetragonal lattice is now larger than the c unit-cell parameter. A similar structural phase

transition from the cubic to a tetragonal phase has already been observed at low temperature (Arima et al.,

2007; Ohtani et al., 2010; Tsuda et al. 2010). With decreasing temperature, the (800) diffraction peak of

the cubic phase begins to split at 140 K, indicating a cubic to tetragonal phase transition with $c < a$

(Ohtani et al. 2010). According to Ohtani et al. (2010), the tetragonal compression with $c < a$ is

attributable to the anharmonic elastic energy. Compared with the pressure-induced phase transition,

however, there is little change in unit-cell volume regardless of the tetragonal compression. The crystal

structure changes further to orthorhombic at 70 K, the ferromagnetic transition temperature (Arima et al.

2007; Ohtani et al. 2010). The variation in unit-cell parameters during the pressure-induced phase

transition of ulvöspinel is similar to that of chromite in that $c < a$ in the tetragonal phase, whereas the low

temperature phase transition in the ulvöspinel results instead in a unit cell with $c > a$ (Yamanaka et al.

2009).

Crystal structures

The normal spinel-type structure $A^{2+}B^{3+}_2O_4$ consists of a cubic close-packed arrangement of oxygen atoms in which one half of the octahedral sites are occupied with trivalent B^{3+} cations and one eighth of the tetrahedral sits are occupied by divalent A^{2+} cations. The commonly used setting with an inversion center at the origin is employed with the tetrahedral cation at (1/8,1/8,1/8) and the octahedral cation at (1/2,1/2,1/2). The oxygen positional parameter in this setting is at u,u,u ($u \sim 0.25$). A structure determination for chromite at ambient conditions resulted in a value for the oxygen positional parameter of 0.2624 (4). This value is near that for $MgAl_2O_4$ spinel, which has $u = 0.2633$ (3) (Finger et al. 1986). The u parameter for an ideally closed packed anion configuration is 0.25, which suggests that the CrO_6 octahedron is distorted along the [111] axis in $FeCr_2O_4$. That is, the O-Cr-O bond angles in the octahedron are 96.1 (2)° and 83.9 (2)° (Table 1) and differ, therefore, from those in a regular octahedral geometry. It is worth noting that the Fe-O bond distance in the FeO_4 tetrahedron in chromite is 1.996 (6) Å, which is almost equal to the Cr-O bond distance 1.997 (3) Å in the CrO_6 octahedron (Table 1). The tetrahedral Fe-O and the octahedral Cr-O bond distances obtained are in good agreement with the previously reported Fe-O bond distance, 1.997 (1) Å, and Cr-O bond distance, 1.994 (1) Å (Lenaz et al. 2004). The fact that the two types of polyhedra in chromite have similar bond lengths despite differences in coordination is attributable to the large size of the Fe^{2+} cation ($^{IV}Fe^{2+} = 0.63$ Å, $^{VI}Cr^{3+} = 0.615$ Å; Shannon (1976)). The variation in polyhedral volumes and bond distances as a function of pressure are shown in Figures 3 (c) and (d). In chromite, the FeO_4 tetrahedron and the CrO_6 octahedron are compressed isotropically with pressure (Fig. 3 (c)) with their Fe-O and Cr-O bond distances decreasing smoothly from 1.996 (6) to

1.949 (7) Å and from 1.997 (3) to 1.969 (7) Å, respectively (Fig. 3 (d)). With isotropic contraction of the regular tetrahedron, however, the bond angle in the CrO_6 octahedron is decreased from 96.1 (2)° to 95.7 (4)° with increasing pressure. The same behavior has been observed in spinel (Finger et al. 1986) and ulvöspinel (Yamanaka et al. 2009), which both have the normal spinel structure with deformed octahedra. The octahedra in magnetite, on the other hand, remain essentially unchanged with respect to distortion (Finger et al. 1986; Gotta et al. 2007). A least-squares fit of the Birch-Murnaghan EoS to these polyhedra in chromite yields $V_0 = 4.07$ (1) $Å^3$, $K_0 = 147$ (9) GPa (fixed $K' = 4.0$) for the tetrahedron and $V_0 = 10.42$ (2) $Å^3$, $K_0 = 275$ (24) GPa (fixed $K' = 4.0$) for the octahedron, indicating that the FeO_4 tetrahedron is more compressible than the CrO_6 octahedron (Fig. 3 (c)). Most oxide spinels have similar bulk moduli (about 200 GPa), because the observed bulk modulus indicates an average of polyhedral compressibilities between the tetrahedron and octahedron in the spinel structure (Finger et al. 1986). In chromite, the large tetrahedral compressibility is compensated by a low octahedral compressibility. Bulk moduli of polyhedra in ulvöspinel, which has a tetrahedral site fully occupied by Fe^{2+}, are $V_0 = 11.21$ (1) $Å^3$, $K_0 = 237$ (10) GPa (fixed $K' = 4.0$) for the octahedron and $V_0 = 4.17$ (2) $Å^3$, $K_0 = 155$ (39) GPa (fixed $K' = 4.0$) for the tetrahedron. It is noteworthy that the tetrahedron in ulvöspinel has a similar compressibility to that in chromite (Table 3). The difference in crystal bulk modulii between chromite ($K_0 = 209$ (13) GPa) and ulvöspinel ($K_0 = 185$ (20) GPa) is due to the difference in octahedral compressibility between CrO_6 ($K_0 = 275$ (24) GPa) and TiO_6 ($K_0 = 237$ (10) GPa).

The present data show little bond length distortion in the FeO_4 tetrahedra throughout the pressure

range studied. At the phase transition boundary, however, in the octahedron, the two Cr-O bonds parallel to the c-axis shorten from 1.969 (7) Å to 1.922 (17) Å and the other four Cr-O bonds parallel to the ab plane elongate from 1.969 (7) Å to 1.987 (9) Å (Fig. 3 (d)). This anisotropic deformation leads to the tetragonal compression along the c-axis. Bond angle variance parameters defined by Robinson et al. (1971) are also listed in Table 1. The angular distortion is defined as the amount of deviation from the ideal bond angle for a regular polyhedron. The angular distortion of the octahedron decreases continuously up to 13.7 GPa (Fig. 3 (e)). On the other hand, the angular distortion in tetrahedron rises dramatically after the phase transition (Fig. 3 (e)). This observation suggests that an activation of the Jahn-Teller effect at Fe^{2+} with pressure gives rise to this tetrahedral angular distortion, which is responsible for the cubic-to-tetragonal phase transition.

Very recently, 3d orbital ordering in the tetragonal $FeCr_2O_4$ phase has been directly observed at low temperature by convergent-beam electron diffraction (CBED) (Tsuda et al. 2010). Compared with the FeO_4 tetrahedra in the high-pressure phase of chromite, those in the low temperature phase are "flattened" along the c direction, with the tetrahedral bond angle along the c-axis direction increasing from the ideal value of 109.5° to 111.8° (Tsuda et al. 2010). It has been suggested that the 3d electrons of Fe^{2+}, which contribute to the Jahn-Teller effect, are ordered into the dz^2 orbital along the c-axis at low temperature. In the tetragonal $FeCr_2O_4$ phase at high pressure, on the other hand, the tetrahedral bond angle along the c-axis direction decreases from 109.5° to 106.6 (7)° with pressure (Table 1), which leads to a "stretched" tetrahedral geometry.

The change in coordination geometry with increasing pressure in chromite can be understood on the basis of qualitative molecular orbital considerations. In chromite, the tetrahedra should behave as isolated molecular units in the solid, because they do not share any vertices with each other. According to the Jahn-Teller theorem (Jahn and Teller, 1937) high-spin Fe^{2+} with a d^6 electronic configuration in a site of tetrahedral symmetry leads to an orbitally degnerate ^2E electronic state, as shown in Figure 4 (center), with the familiar pattern of e and t_2 (metal-oxygen antibonding) orbitals appropriate for a tetrahedral unit. The Jahn-Teller theorem, however, does not allow an *a priori* prediction of the geometry of the distorted molecule, but only states that the molecule must distort to a lower symmetry in order to remove the degeneracy. Application of standard group theoretical techniques to the problem of tetrahedrally-coordinated Fe^{2+}, as outlined in Burdett (1980) shows that the only available normal vibrational mode that can distort the ideal tetrahedron and lower its symmetry is a vibration of E symmetry, which will lead to one of two distorted tetrahedra with point group D_{2d} (Fig. 4 left, "flattened geometry;" right, "stretched" geometry). In either case, the orbital degeneracy has been removed by the distortion.

When the molecule is distorted from T_d to D_{2d} symmetry, the t_2 orbital set splits into e (dxz, dyz) + b_2, (dxy) whereas the e orbital set splits into b_1 (dx^2-y^2) + a_1 (dz^2). As the distortion proceeds toward either the elongated or flattened tetrahedral geometry, the orbital sets split in opposite fashion depending on the nature of the distortion. This qualitative picture agrees with the electron diffraction experiments of Tsuda, et al. (2010), in which it was observed that at low temperature ("flattened" tetrahedra), an increased

electron density was ascribed to the dz^2 orbital, which is lower in energy and is doubly occupied as result of the distortion. In a tetrahedral unit with a Jahn-Teller unstable ion at the coordination center, the 3d orbitals are not pointed directly at the oxygen atoms, as is the case in an octahedral molecule. This type of distortion is often referred to as "dynamic," in contrast to the "static" distortion observed in octahedral copper (II) compounds with the d^9 configuration, for example. Similar effects occur in octahedral molecules in which the orbital degeneracy originates in the t_{2g} orbital set, whose 3d orbitals do not point directly at the ligands. In both cases, distortions are not generally observable on the time scale of the diffraction experiment except at sufficiently low temperature. The former situation appears to be the case for the FeO_4 tetrahedron in chromite. On the other hand, optical absorption experiments have shown some splitting of the spectral band corresponding to the $^5E \longrightarrow {}^5T_2$ absorption (Slack et al., 1966, Taran and Langer 2001), suggesting that the Jahn-Teller distortion is in fact observable on the time scale of the optical measurement.

Energetically, the two available distortions of the tetrahedron are equivalent to first order. The preference of the tetrahedron for the flattened geometry over the stretched geometry at ambient pressure is a result of a second-order mixing of the higher-lying Fe 4s orbital into the Fe 3d-based molecular orbitals of the tetrahedron. Because the Fe 4s orbital has a_1 symmetry, it can mix on distortion with the dz^2 orbital. This mixing has the effect of further lowering the energy of the dz^2 orbital, while raising the energy of the Fe 4s orbital and providing additional stability to the flattened tetrahedron over the stretched tetrahedron. In the stretched geometry, the dz^2 (a1) orbital will also be afforded some additional stability

from the second-order mixing of the Fe 4s orbital for similar reasons, but this will only serve to offset the destabilization of dz^2 that arises from the stretched distortion. A similar phenomenon has been proposed to account for the observation of the elongated tetragonal distortion of the octahedra in copper (II) compounds (Burdett, 1981).

With increasing pressure, the Fe-O distance in the FeO_4 tetrahedron decreases, leading to a destabilization of all five Fe 3d-O 2p antibonding orbitals. The diffraction data also show, however, that the FeO_4 tetrahedron remains regular up to the pressure of the cubic-tetragonal transition. Although the regular tetrahedron represents the equilibrium configuration of the nuclei below this pressure, the five antibonding orbitals will respond differently to a decreasing Fe-O distance. Figure 5 shows the main Fe 3d-O 2p interactions for each of these five antibonding orbitals in the ideal tetrahedral configuration. Comparing Fig. 5 (a) and (b), it is apparent that the interactions between the Fe $3dz^2$ orbital and the O $2p_z$ orbital shown in (a) are more direct than the interactions between the Fe $3dx^2-y^2$ orbital and the O $2p_y$ orbital shown in (b). Even though there will be a linear combination of the O $2p_x$ and O $2p_y$ that will increase the overall interaction between the 2p orbitals on oxygen and Fe 3d x^2-y^2, the overlap between the dz^2 orbital and O $2p_z$ orbitals is significantly greater. The result of this difference in overlap character is that the dz^2 orbital will be destabilized to a greater degree than the dx^2-y^2 orbital with decreasing Fe-O distance, as shown in the bottom portion of Fig. 6.

Similarly, the overlaps between the dxz and dyz orbitals on Fe (Fig. 5 (d) and (e)) with the corresponding orbitals on the oxygen atoms are more direct than the overlap between the dxy orbital on

Fe with its corresponding O 2p orbitals. (Fig. 5 (c). With decreasing Fe-O distance at high pressure, the d_{xz} and d_{yz} orbitals will split from the d_{xy} orbital to form a pair of e symmetry, while the d_{xy} orbital becomes singly degenerate with b_2 symmetry. By virtue of its more direct overlap with the 2p orbitals on oxygen, the doubly degenerate pair is destabilized to a greater extent than the b_2 orbital as the Fe-O distance decreases, as shown in the top portion of Fig. 6. At high pressure, the Fe 3d-based molecular orbitals of the tetrahedron therefore energetically favor the arrangement corresponding to the stretched tetrahedral geometry as a necessary consequence of the decreasing Fe-O distance at sufficiently high pressure.   As in the case of the "freezing in" of the flattened geometry at low temperature, a critical pressure is required to observe the stretched distortion on the time scale of diffraction measurements.   In the case of high pressure, however, only the "stretched" mode is available to the FeO_4 tetrahedron, and this mode is constrained by symmetry.

It should be noted here that it is the fact that the FeO_4 tetrahedra are isolated within the chromite structure allows an analysis of the Jahn-Teller effect using molecular considerations only. This approach may not be appropriate for the tetrahedral Fe^{2+} ion in crystal structures with more complicated polyhedral arrangements, where additional considerations encompassing the entire crystal structure must be applied. The present result, however, can provide a starting point for such further analyses.

Concluding Remarks

We have shown that the crystal structure of chromite is transformed from a cubic to a tetragonal

structure between 11.8 GPa and 12.6 GPa. Structural refinements show that the FeO_4 tetrahedra and CrO_6 octahedra are compressed isotropically in the cubic spinel structure. Above the phase transition boundary, however, the two Cr-O bonds parallel to the *c*-axis shorten from 1.969 (7) Å to 1.922 (17) Å and the other four Cr-O bonds parallel to *ab* plane elongate from 1.969 (7) Å to 1.987 (9) Å. On the other hand, the tetrahedral bond angles along the *c*-axis begin decreasing from 109.5° to 106.6 (7)° after the phase transition, which generates a stretched tetrahedral geometry. The angular distortion in the octahedron continuously decreases up to 13.7 GPa, whereas the values in tetrahedron dramatically increase after the phase transition. It is proposed that the Jahn-Teller effect at the tetrahedrally-coordinated Fe^{2+} cation becomes active with compression and gives rise to the tetrahedral angular distortion observed in the crystal structure, leading to the observed phase transition.

Acknowledgements

References

Akaogi M, Hamada Y, Suzuki T, Kobayashi M, Okada M (1999) High pressure transitions in the system

$MgAl_2O_4$-$CaAl_2O_4$: a new hexagonal aluminous phase with implication for the lower mantle. Phys

Earth Planet Inter 115: 67–77

Angel RJ (2002) EOSFIT v5.2. Crystallography Laboratory, Virginia Tech, Blacksburg VA.

Angel RJ (2004) Absorption corrections for diamond-anvil cells implemented in the software package

ABSORB 6.0. J Appl Cryst 37: 486–492

Arima T, Watanabe Y, Taniguchi K, Watanabe M, Noda Y (2007) Effect of Mn-substitution on magnetic

and structural properties in $FeCr_2O_4$. J Magn Magn Mater 310: 807–809

Baur H (1974) The geometry of polyhedral distortions. Predictive relationships for the phosphate group.

Acta Cryst B30: 1195–1215

Bordács S, Varjas D, Kézsmárki I, Mihály G, Baldassarre L, Abouelsayed A, Kuntscher CA, Ohgushi K,

Tokura Y. (2009) Magnetic-order-induced crystal symmetry lowering in ACr_2O_4 ferrimagnetic

spinels. Phys Rev Lett 103: 077205

Buerger JM (1951) Phase Transformation in Solids, Eds. Smoluchowski R, Mayer JE, Weyl WA, New

York, John Wiley & Sons

Burdett JK (1980)   Molecular Shapes, New York, Wiley-Interscience

Burdett JK (1981)   Use of the Jahn-Teller theorem in inorganic chemistry.   Inorg Chem 20:

1959-1962.

Catti M, Fava FF, Zicovich C, Dovesi, R (1999) High-pressure decomposition of MCr_2O_4 spinels (M=Mg,

Mn, Zn) by ab initio methods. Phys Chem Miner 26: 389–395

Chen M, Shu JF, Mao HK, Xie XD, Hemley RJ (2003a) Natural occurrence and synthesis of two new

postspinel polymorphs of chromite. Proc Nat Acad Sci 100: 14651–14654

Chen M, Shu JF, Xie XD, Mao HK (2003b) Natural $CaTi_2O_4$-structured $FeCr_2O_4$ polymorph in the

Suizhou meteorite and its significance in mantle mineralogy. Geochim Cosmochim Acta 67:

3937–3942

Deer WA, Howie RA, Zussman J (1966) An Introduction to the Rock forming Minerals. London,

Longman

Dera P (2007) GSE-ADA and RSV data analysis program for monochromatic single crystal diffraction

with area detector, GeoSoilEnviroCARS, Argonne, Ill

Dera P, Lavina B, Borkowski LA, Prakapenka VB, Sutton SR, Rivers ML, Downs RT, Boctor NZ, Prewitt

CT (2008) High-pressure polymorphism of Fe_2P and its implications for meteorites and Earth's

core. Geophys Res Lett 35: L10301

Dunitz JD, Orgel LE (1960) Stereochemistry of ionic solids. Adv Inorg Radiochem 2: 1-60

Enomoto A, Kojitani H, Akaogi M, Miura H, Yusa H (2009) High-pressure transitions in $MgAl_2O_4$ and a

new high-pressure phase of $Mg_2Al_2O_5$. J Solid State Chem 182: 389–395

Fan D, Zhou W, Liu C, Liu Y, Jiang X, Wan F, Liu J, Li X, Xie H (2008) Thermal equation of state of

natural chromium spinel up to 26.8 GPa and 628 K. J Mat Sci 43: 5546–5550

Fei Y, Frost DJ, Mao HK, Prewitt CT, Häusermann D (1999) In situ determination of the high-pressure

phase of Fe_3O_4. Am Mineral 84: 203–206

Finger LW, Hazen RM, Hofmeister AM (1986) High-Pressure crystal chemistry of spinel ($MgAl_2O_4$) and

magnetite (Fe_3O_4): Comparisons with silicate spinels. Phys Chem Miner 13: 215–220

Fleet M.E, Angeli N, Pan Y (1993) Oriented chlorite lamellae in chromite from the Pedra Branca

mafic-ultramafic complex, Ceara, Brazil. Am Mineral 78: 68–74

Gillet P, Fiquet G, Daniel I, Reynard B, Hanfland M (1999) Equations of state of ^{12}C and ^{13}C diamond.

Phy Rev B 60: 14660–14664

Goodenough JB (1964) Jahn-Teller distortions induced by tetrahedral-site Fe^{2+} ions. J Phys Chem Solids

25: 151–160

Haavik C, Stølen S, Fjellvåg H, Hanfland M, Häusermann D (2000) Equation of state of magnetite and its

high-pressure modification: Thermodynamics of the Fe-O system at high pressure. Am Mineral

85: 514–523

Hammersley AP (1998) FIT2D v.9.129 Reference Manual v.3.1

Holland TJB, Redfern SAT (1997) Unit cell refinement from powder diffraction data: the use of

regression diagnostics. Mineral Mag 61: 65–77

Izumi F, Ikeda T (2000) A Rietveld-analysis program RIETAN-98 and its application to zeolites. Mater

Sci Forum, 321-324, 198-203.

Jahn, H. A. and Teller, E. (1937) Stability of polyatomic molecules in degenerate electronic states I.

orbital degeneracy, Proceedings of the Royal Society of London, Series A, 161, 220-235.

Katsura T, Yamada H, Shinmei T, Kubo A, Ono S, Kanzaki M, Yoneda A, Walter MJ, Ito E, Urakawa S, Funakoshi K, Utsumi W (2003) Post-spinel transition in Mg_2SiO_4 determined by high P-T in situ X-ray diffractometry. Phys Earth Planet Int 136: 11–24

King HE, Finger LW (1979) Diffracted beam crystal centering and its application to high-pressure crystallography. J Appl Cryst 12: 374–378

Lenaz D, Skogby H, Princivalle F, Halenius U (2004) Structural changes and valence states in the $MgCr_2O_4$–$FeCr_2O_4$ solid solution series. Phys Chem Miner 31: 633–642

Lenaz D, Braidotti R, Princivalle F, Garuti G, Zaccarini F (2007) Crystal chemistry and structural refinement of chromites from different chromitite layers and xenoliths of the Bushveld Complex. Eur J Mineral 19: 599–609

Lenaz D, Logvinova AM, Princivalle F, Sobolev NV (2009) Structural parameters of chromite included in diamond and kimberlites from Siberia: A new tool for discriminating ultramafic source. Am Mineral 94: 1067–1070

Levy D, Pavese A, Hanfland M (2000) Phase transition of synthetic zinc ferrite spinel ($ZnFe_2O_4$) at high pressure from synchrotron X-ray powder diffraction. Phys Chem Miner 27:638–644

Levy D, Diella V, Dapiaggi M, Sani A, Gemmi M, Pavese, A (2004) Equation of state, structural behaviour and phase diagram of synthetic $MgFe_2O_4$, as a function of pressure and temperature. Phys Chem Miner 31: 122–129

Mao HK, Xu J, Bell PM (1986), Calibration of the ruby pressure gauge to 800 kbar under

quasi-hydrostatic conditions. J Geophys Res 91: 4673–4676

Melcher F, Grum W, Simon G, Thalhammer TV, Stumpfl EF (1997) Petrogenesis of the ophiolitic giant

chromite deposits of Kempirsai, Kazakhstan: a study of solid and fluid inclusions in chromite. J

Petrol 38: 1419–1458

Ohgushi K, Okimoto Y, Ogasawara T, Miyasaka S, Tokura Y (2008) Magnetic, optical, and

magnetooptical properties of spinel-type ACr_2X_4 (A = Mn, Fe, Co, Cu, Zn, Cd; X = O, S, Se). J

Phys Soc Jpn 77: 034713

Ohtani S, Watanabe Y, Saito M, Abe N, Taniguchi K, Sagayama H, Arima T, Watanabe M, Noda Y (2010)

Orbital dilution effect in ferrimagnetic $Fe_{1-x}Mn_xCr_2O_4$: Competition between anharmonic lattice

potential and spin-orbit coupling. J Phys Condens Matter 22: 176003

Peltier WR, Solheim LP (1992) Mantle phase-transitions and layered chaotic convection. Geophys Res

Let 19: 321–324

Robinson K, Gibbs GV, Ribbe PH (1971) Quadratic elongation: a quantitative measure of distortion in

coordination polyhedra. Science 172: 567–570

Shannon RD (1976) Revised effective ionic radii and systematic studies of interatomic distances in

halides and chalcogenides. Acta Cryst A32: 751-767

Sheldrick GM (1997) SHELXL97, Release 97-2. Program for the refinement of crystal structures.

University of Göttingen, Germany.

Shim SH, Duffy TS, Shen GY (2001) The post-spinel transformation in Mg_2SiO_4 and its relation to the

660-km seismic discontinuity. Nature 411: 571–574

Shu JF, Mao WL, Hemley RJ, Mao HK (2007) Pressure-induced distortive phase transition in chromite-spinel at 29 GPa. Materials Research at High Pressure, eds. Manaa MR, Goncharov AF, Hemley RJ, Bini R, 987: 179–184, Warrendale, PA, Materials Research Society

Slack GA, Ham FS, Chrenko RM (1966) Optical absorption spectra of tetrahedral Fe^{2+} ($3d^6$) in cubic ZnS, CdTe and $MgAl_2O_4$.   Phys. Rev 152: 376-402

Taran MN, Langer K (2001) Electronic absorption spectra of Fe^{2+} ions in oxygen-based rock-forming minerals at temperatures between 297 and 600 K. Phys. Chem. Minerals 28: 199-210

Tomiyasu K, Hiraka H, Ohoyama K, Yamada K (2008) Resonance-like magnetic excitations in spinel ferrimagnets $FeCr_2O_4$ and $NiCr_2O_4$ observed by neutron scattering. J Phys Soc Jpn 77: 124703

Tsuda K, Morikawa D, Watanabe Y, Ohtani S, Arima T (2010) Direct observation of orbital ordering in the spinel oxide $FeCr_2O_4$ through electrostatic potential using convergent-beam electron diffraction. Phys Rev B 81; 180102

Yamanaka T, Uchida H, Nakamoto Y (2008) Structural transition of post-spinels, $CaTi_2O_4$, $CaMn_2O_4$ and $CaFe_2O_4$ under high pressures up to 80 GPa. Am Mineral 93: 1874–1881

Yamanaka T, Mine T, Asogawa S, Nakamoto Y (2009) Jahn-Teller transition of Fe_2TiO_4 observed by maximum entropy method at high pressure and low temperature. Phys Rev B80: 134120

Figure 1 Selection of powder x-ray diffraction patterns of chromite at different pressures up to 17.9 GPa. The background was subtracted in all spectra. Pressures are indicated in the plot. Extra peaks are indicated by arrows.

Figure 2 Rietveld refinement of $FeCr_2O_4$ diffraction pattern measured at 17.9 GPa.

Figure 3 The structural parameter variations with increasing pressure up to 13.7 GPa determined by the single-crystal X-ray diffraction. (a) The volume compression curve: the volume of the tetragonal lattice is doubled, (b) unit cell parameters: the a lattice constant values in tetragonal phase are multiplied by $\sqrt{2}$, (c) the compression curves of tetrahedron and octahedron, (d) the T-O and M-O bond distances, (e) tetrahedral and octahedral angular distortions.

Figure 4 Section of the full molecular orbital diagram of the FeO_4 tetrahedral unit showing the qualitative energy shifts of the Fe d-orbitals of the ideal (T_d) structure, arising from normal modes of E symmetry as a result of a Jahn-Teller instability. In the splitting of the t_2 orbital set, the doubly-degenerate e pair is raised or lowered half as much in energy as the singly-degenerate b_2 orbital, leading to the first-order energetic equivalence of the two possible distortion modes.

Figure 5 Principal orbital interactions contributing to the overlap of Fe 3d orbitals with O 2p orbitals in the tetrahedral FeO_4 unit. For the sake of clarity, only one orbital of the O $2p_x$, O $2p_y$ pair is shown, although in each case where an O $2p_x$ orbital has a contribution, the corresponding O $2p_y$ orbital also may interact, and vice versa

Figure 6 Destabilization of the Fe 3d-based molecular orbitals of the FeO_4 tetrahedral unit with pressure, leading to the orbital energy level scheme for the stretched tetrahedron.

LIST OF TABLE CAPTIONS

Table 1   The structural refinement parameters, the unit-cell parameters, and crystal structure data

of $FeCr_2O_4$ at each pressure.

Table 2   Observed and predicted EoS parameters for ferric, ferrous, and chromium spinels.

Table 3   Observed EoS parameters for tetrahedra and octahedra in spinels.
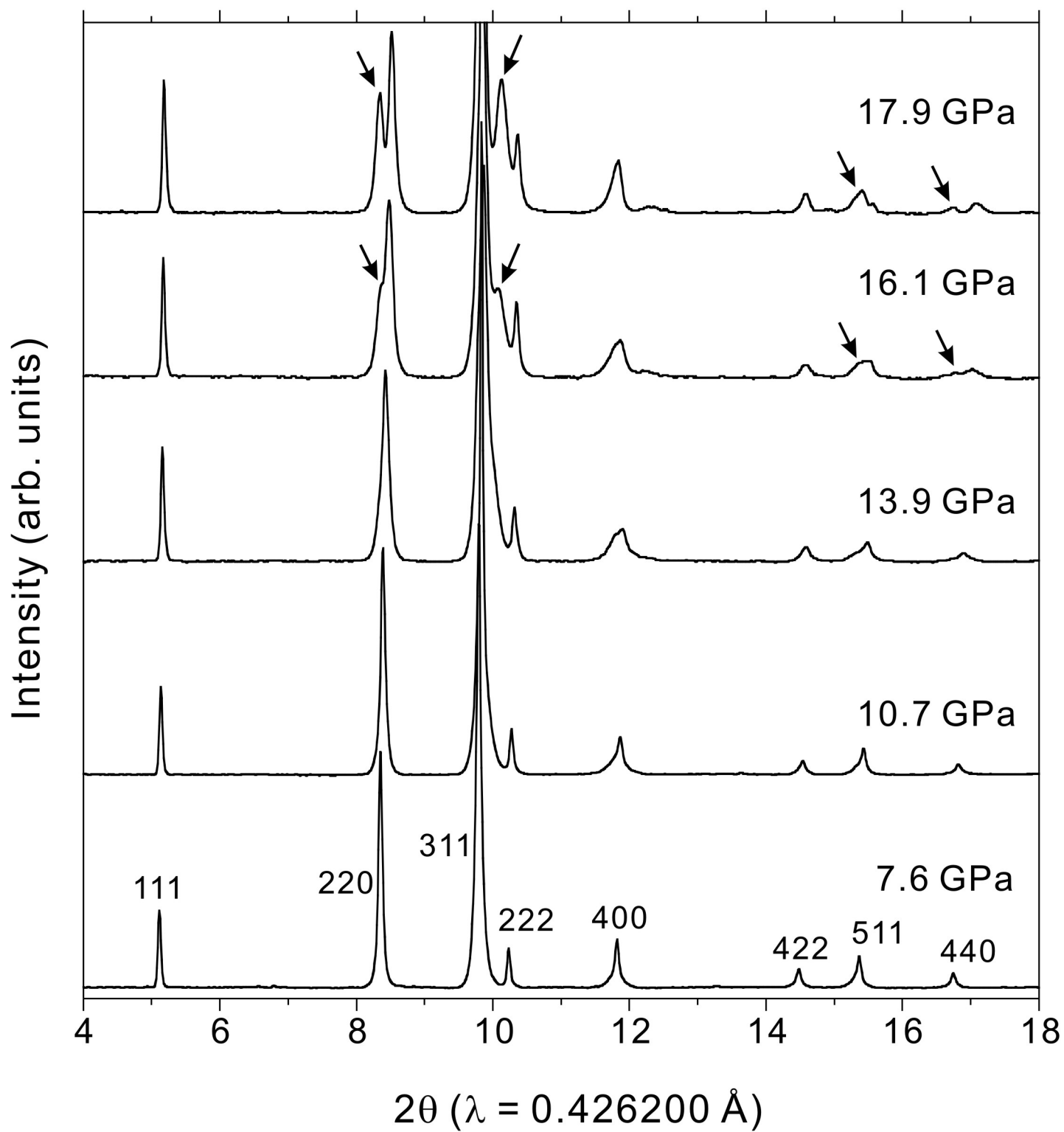
Figure 1
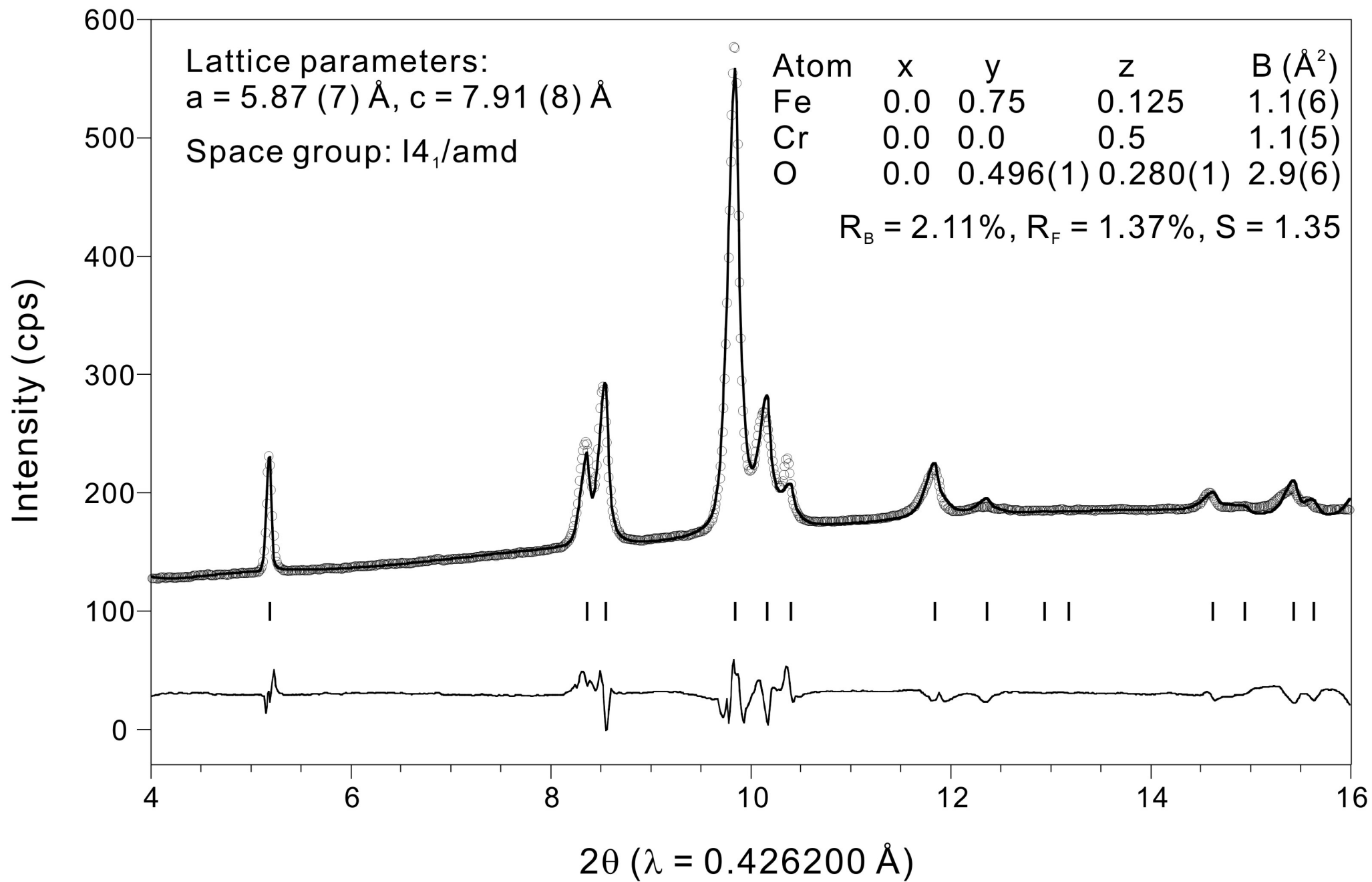
Figure 2
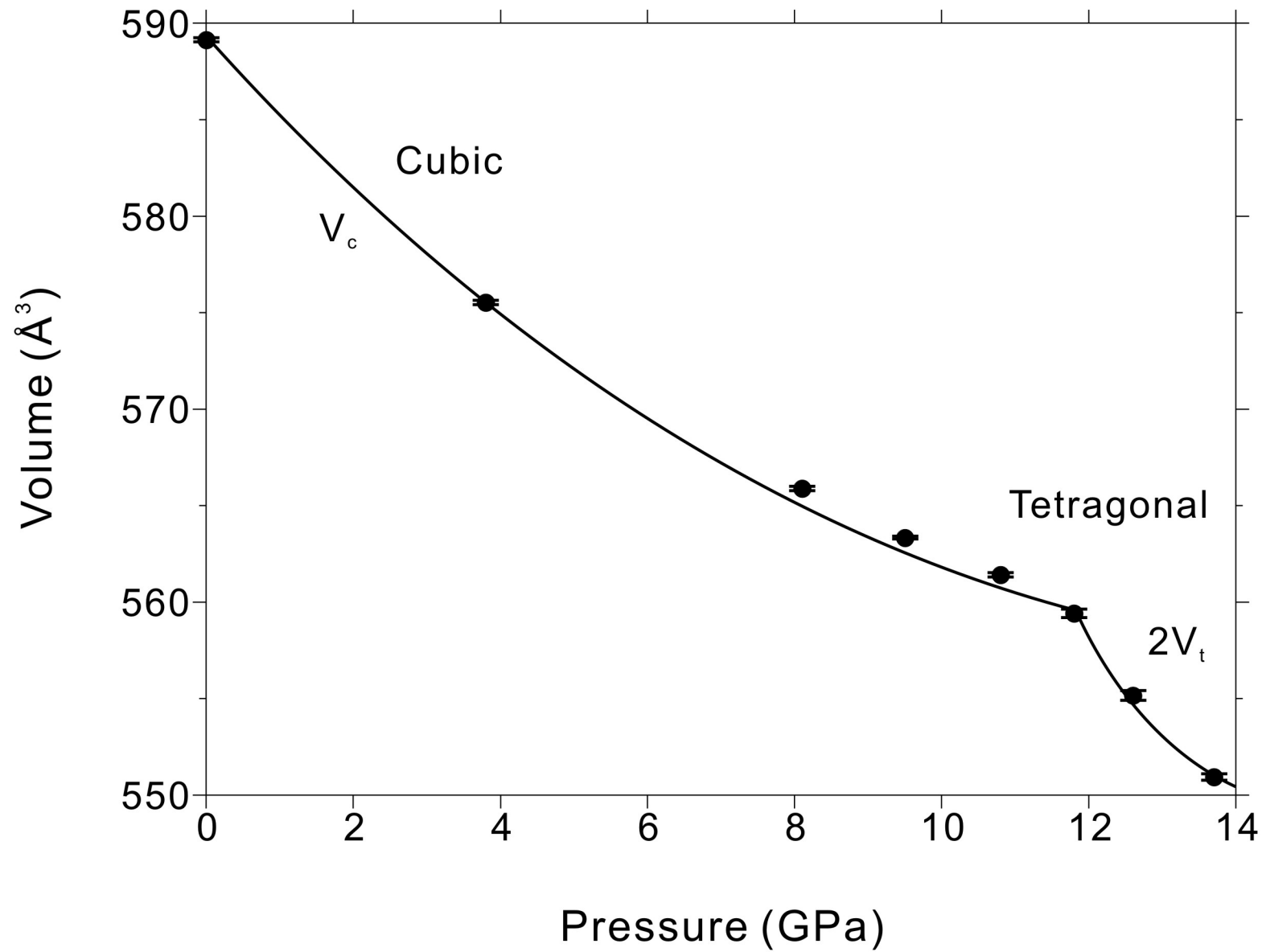
Figure 3a
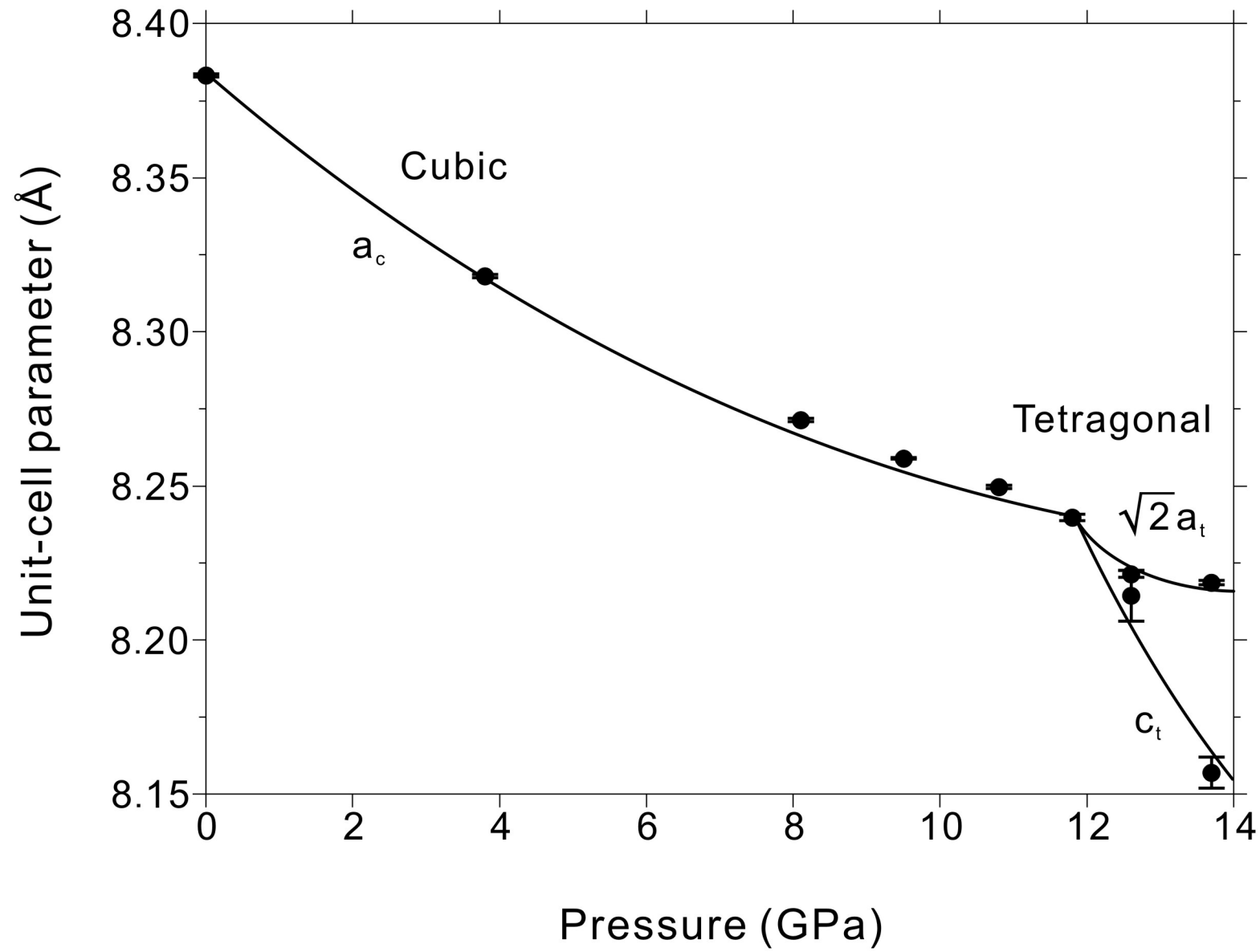
Figure 3b
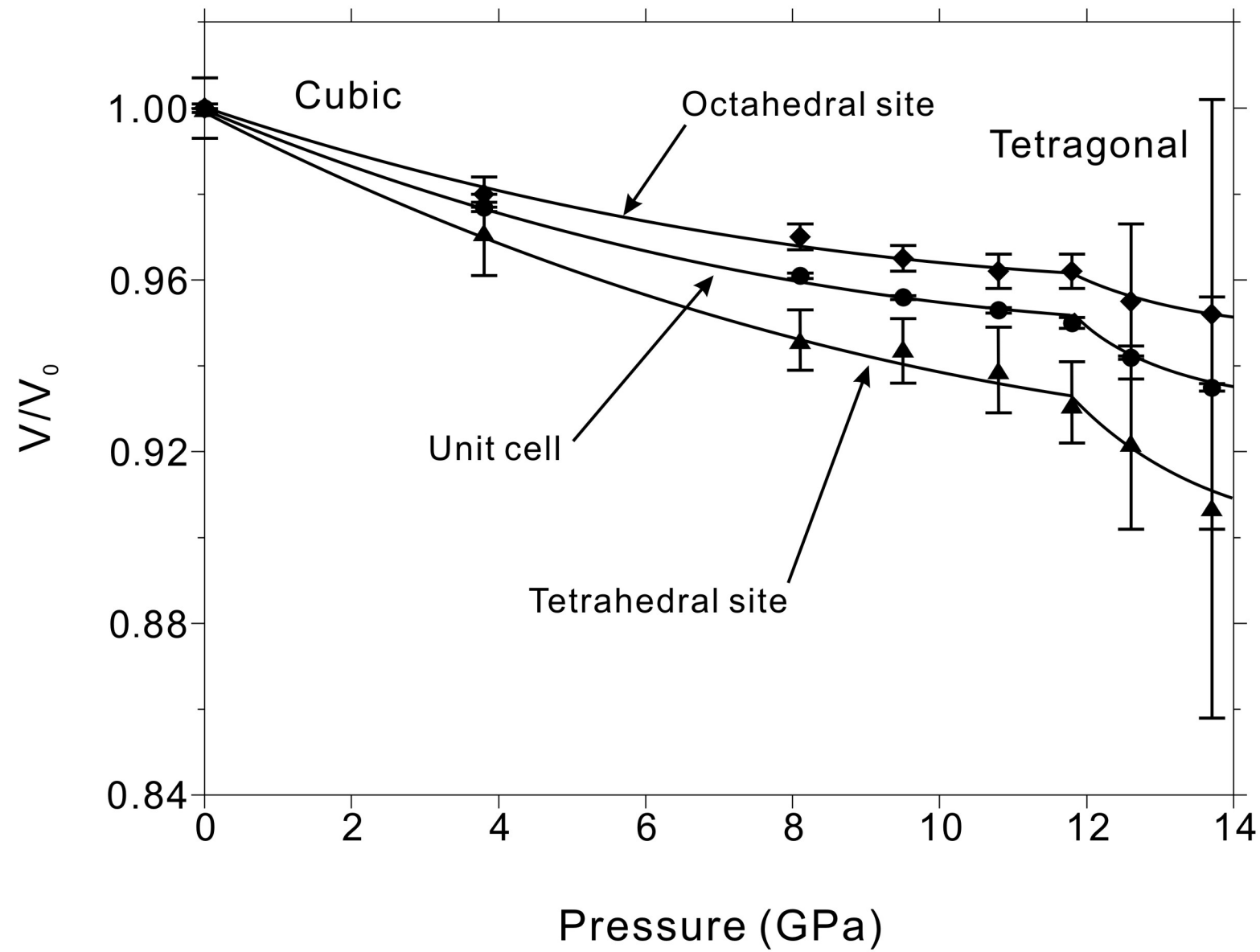
Figure 3c
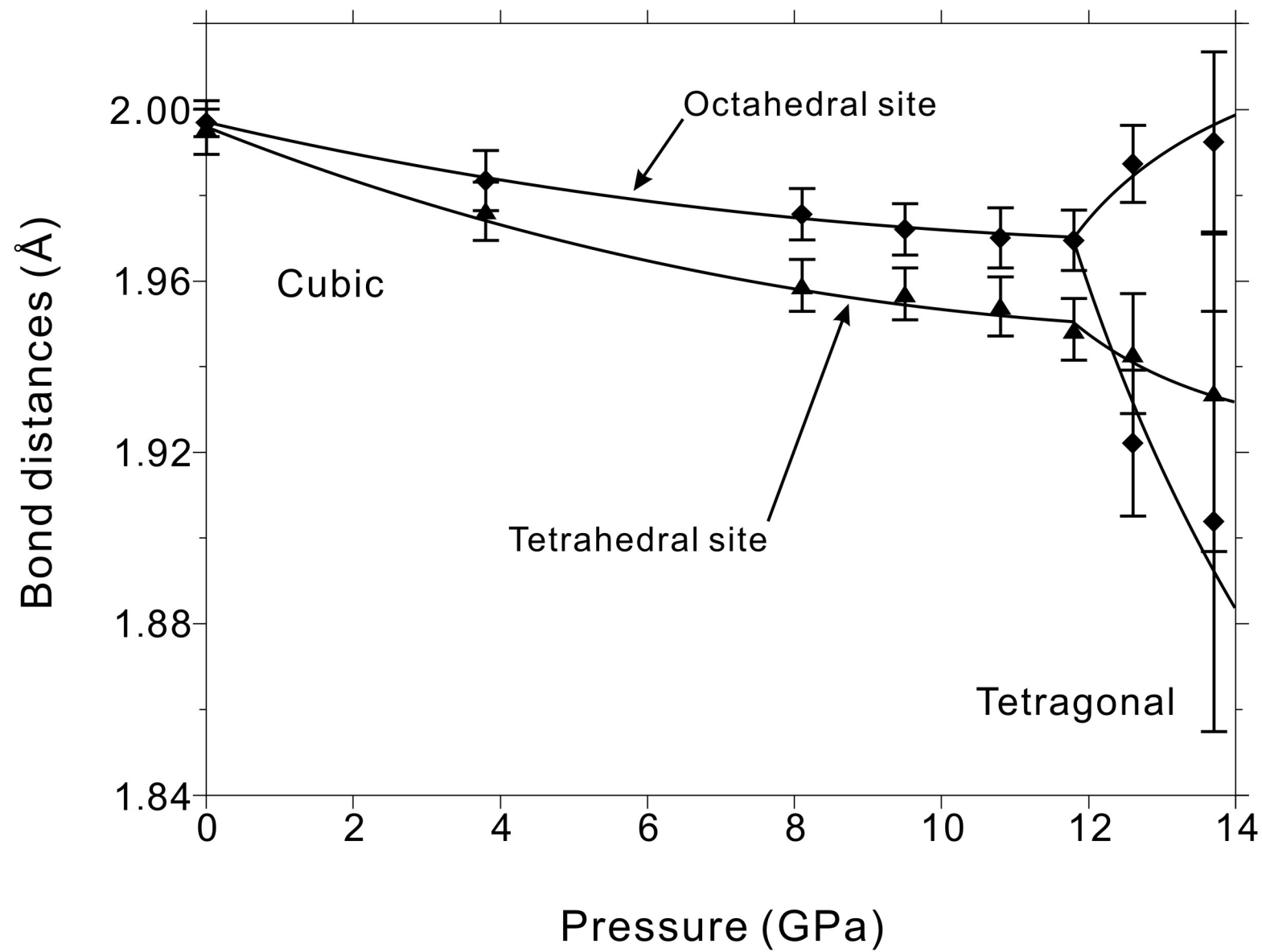
Figure 3d

Figure 3e

Figure 4

c

d

e

z
y
x

a

b
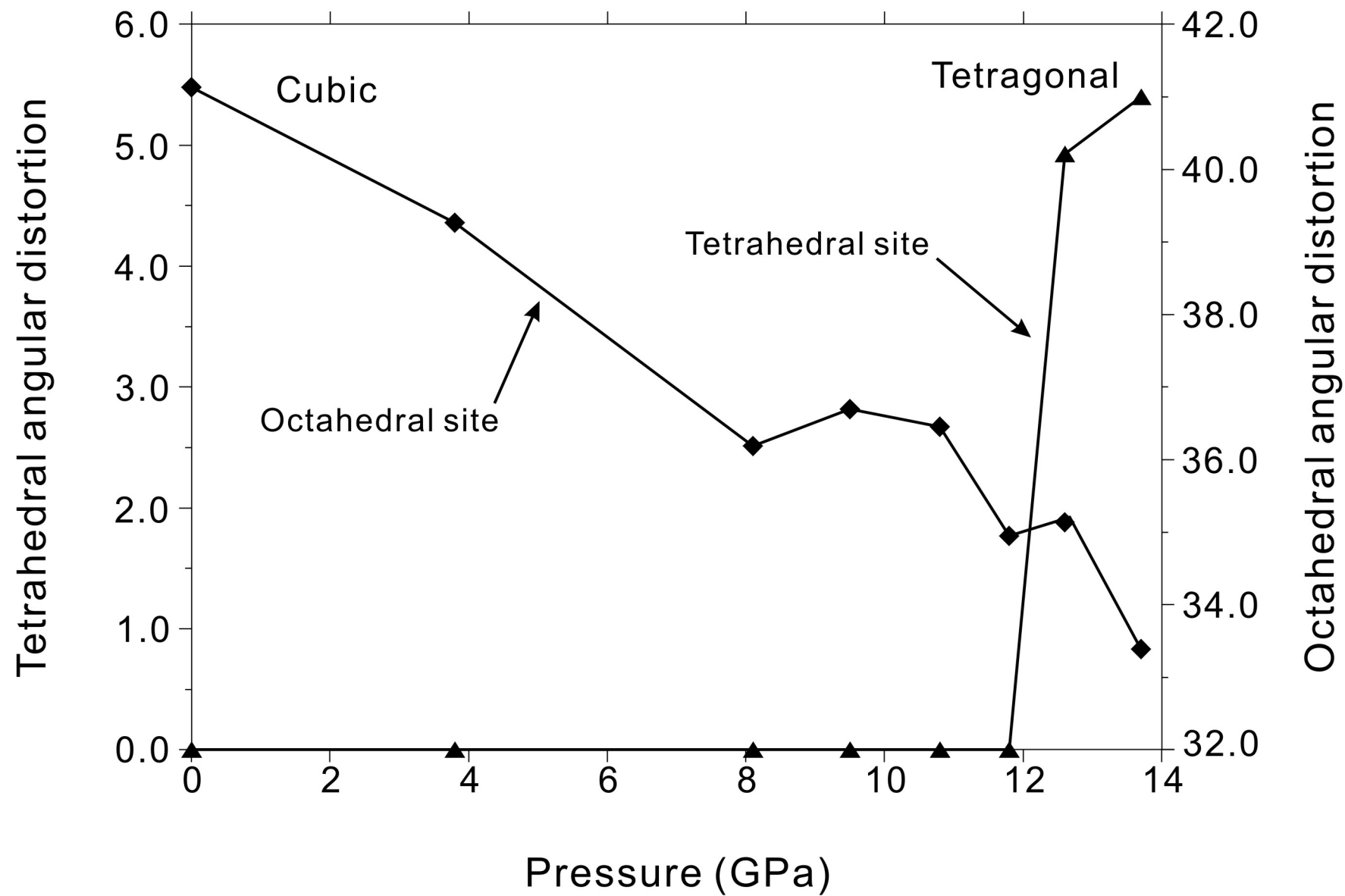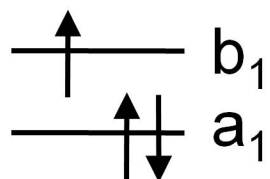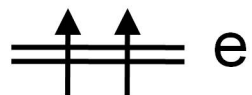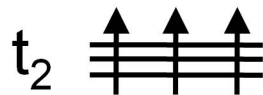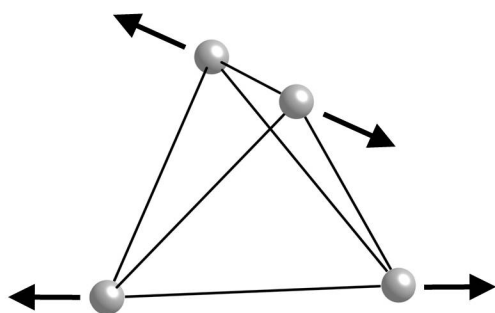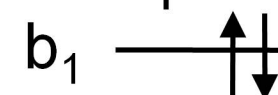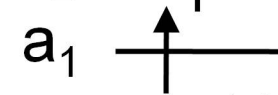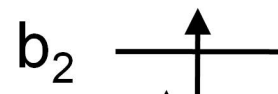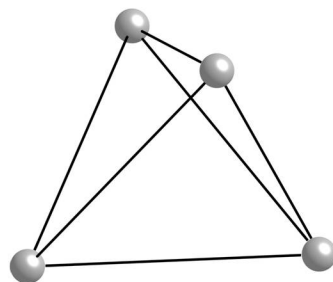
Figure 5

Figure 6

Table 1 The structural refinement parameters, the unit-cell parameters, and crystal structural data of $FeCr_2O_4$ at each pressure

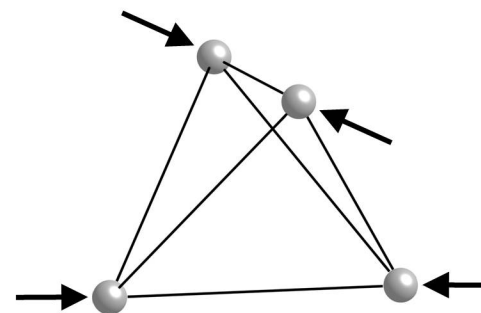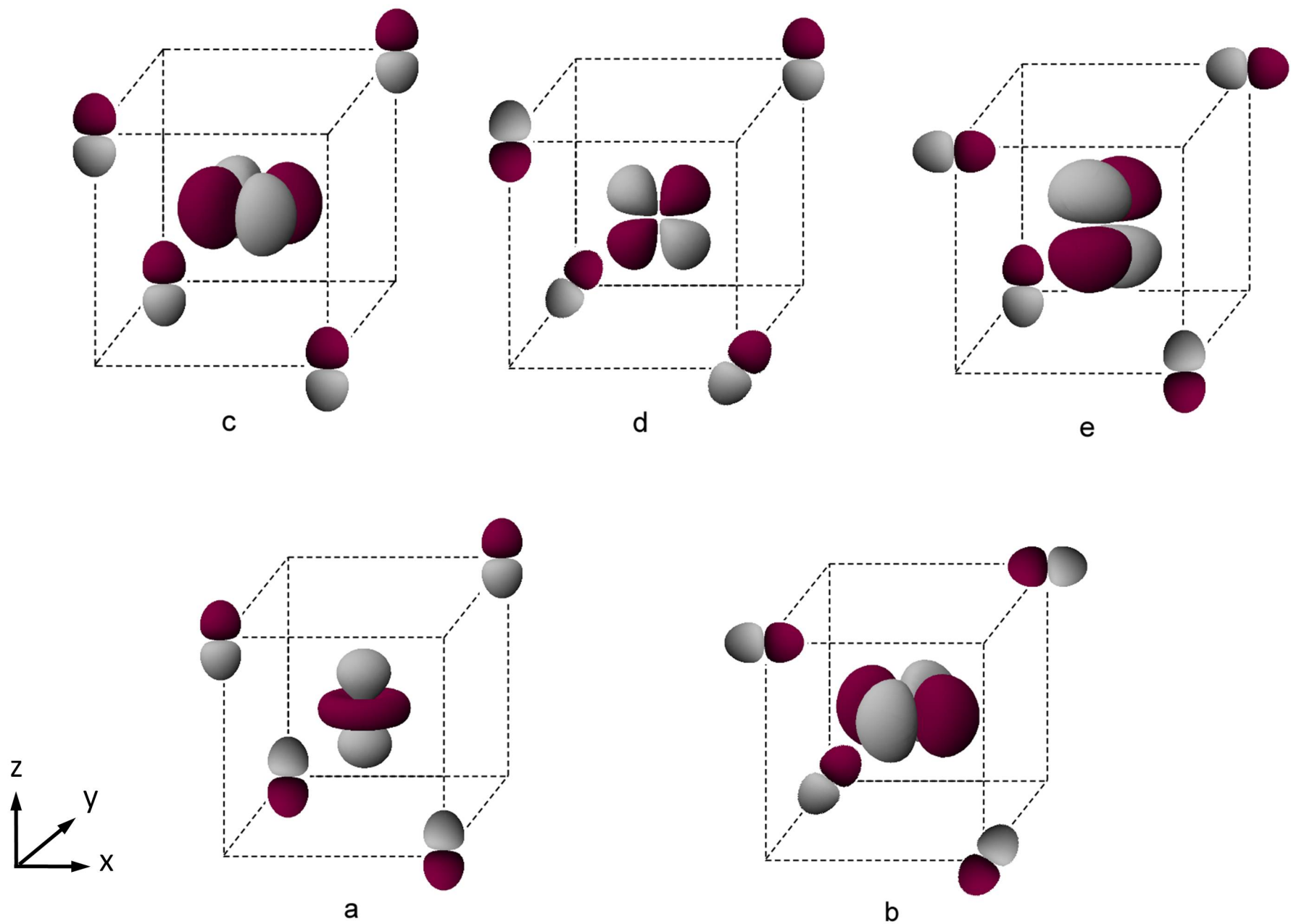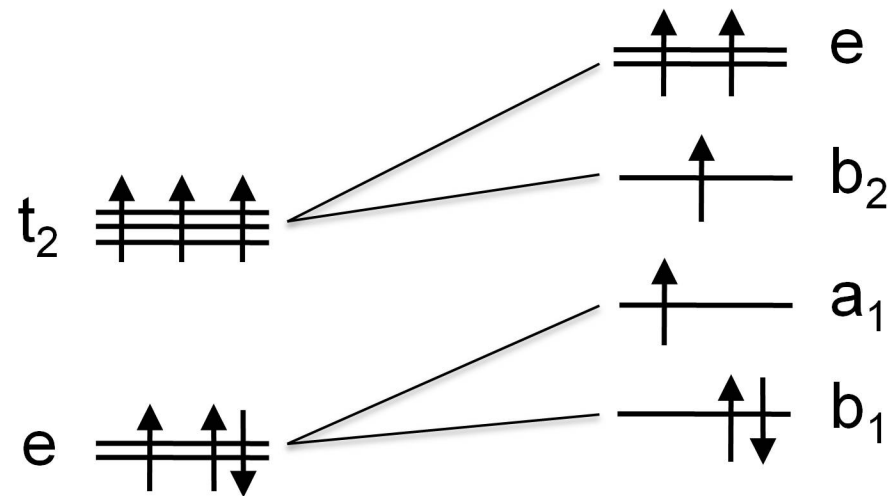| Pressure (GPa)	0.0001 †	3.8	8.1	9.5	10.8	11.8	12.6	13.7
Crystal system	cubic	cubic	cubic	cubic	cubic	cubic	tetragonal	tetragonal
Space group	$Fd-3m$	$Fd-3m$	$Fd-3m$	$Fd-3m$	$Fd-3m$	$Fd-3m$	$I4_1/amd$	$I4_1/amd$
Unit-cell parameters a (Å)	8.3832 (5)	8.3181 (3)	8.2714 (5)	8.2590 (3)	8.2497 (5)	8.2398 (11)	5.8135 (12)	5.8114 (7)
c (Å)							8.2144 (83)	8.1570 (51)
No. of collected reflections	264	36	44	40	39	40	37	32
No. of reflections with $F_o > 4\sigma(F_o)$	58	12	18	19	19	20	16	12
R1 (%)	3.44	3.60	5.36	3.78	4.12	5.05	5.98	7.34
wR2 (%)	6.42	8.12	6.12	8.33	8.07	7.56	13.13	5.56
T (x, y, z)			(1/8, 1/8, 1/8)				(0, 3/4, 1/8)	
M (x, y, z)			(1/2, 1/2, 1/2)				(0, 0, 1/2)	
O x	0.2624 (4)	0.2622 (8)	0.2617 (7)	0.2618 (7)	0.2618 (8)	0.2615 (8)	0.0	0.0
O y	0.2624 (4)	0.2622 (8)	0.2617 (7)	0.2618 (7)	0.2618 (8)	0.2615 (8)	0.482 (2)	0.483 (5)
O z	0.2624 (4)	0.2622 (8)	0.2617 (7)	0.2618 (7)	0.2618 (8)	0.2615 (8)	0.266 (2)	0.267 (6)
$U_{eq}(T)$ (Å^2)	0.0188 (9)	0.0325 (10)	0.0225 (12)	0.0843 (9)	0.0861(10)	0.1085 (11)	0.104 (5)	0.195 (7)
$U_{eq}(M)$ (Å^2)	0.0161 (8)	0.0225 (10)	0.0194 (12)	0.0936 (9)	0.1010 (11)	0.1175 (11)	0.164 (5)	0.171 (6)
$U_{eq}(O)$ (Å^2)	0.0172 (13)	0.0917 (16)	0.1290 (20)	0.1592 (12)	0.1188 (15)	0.1176 (16)	0.143 (10)	0.157 (15)
T-O ×4 (Å)	1.996 (6)	1.976 (7)	1.959 (6)	1.957 (6)	1.954 (7)	1.949 (7)	1.943 (14)	1.934 (37)
O-T-O (°)	109.47	109.47	109.47	109.47	109.47	109.47	106.6 (7)	106.5 (19)
T site volume (Å^3)	4.08 (3)	3.96 (4)	3.86 (3)	3.85 (3)	3.83 (4)	3.80 (4)	3.76 (8)	3.70 (20)
σ^2 (T) ‡	0.00	0.00	0.00	0.00	0.00	0.00	4.93	5.40
M-O ×2 (Å)	1.997 (3)	1.983 (7)	1.976 (6)	1.972 (6)	1.970 (7)	1.969 (7)	1.922 (17)	1.904 (49)
M-O ×4 (Å)	1.997 (3)	1.983 (7)	1.976 (6)	1.972 (6)	1.970 (7)	1.969 (7)	1.987 (9)	1.992 (21)
O-M-O × 2 (°)	96.1 (2)	96.0 (4)	95.8 (3)	95.8 (3)	95.8 (4)	95.7 (4)	94.5 (7)	94.2 (19)
O-M-O × 4 (°)	96.1 (2)	96.0 (4)	95.8 (3)	95.8 (3)	95.8 (4)	95.7 (4)	96.2 (7)	96.1 (20)
M site volume (Å^3)	10.45 (1)	10.24 (4)	10.14 (3)	10.08 (3)	10.05 (4)	10.05 (4)	9.98 (19)	9.95 (52)
σ^2 (M) ‡	41.13	39.27	36.19	36.7	36.45	34.95	35.14	33.39

† This measurement was carried out with a four-circle diffractometer equipped with a scintillation point detector using MoKα radiation ($\lambda = 0.71069$ Å).

‡ Bond angle variance parameter defined by Robinson et al. (1971); $\sigma^2 = \Sigma[(\theta_i - \theta_0)^2/(n - 1)]$, where θ_i is the ith bond angle, θ_0 is the ideal bond angle for a regular polyhedron, and n is the coordination number.

Table 2 Observed and predicted elastic parameters for ferric, ferrous, and chromium spinels.

Spinels Chemical formual	Cations T	M	Calculations	V_0 (Å^3)	K_0 (GPa)	K'	References
$FeCr_2O_4$	Fe^{2+}	Cr^{3+}	BM	588 (1)	209 (13)	4.0 (fixed)	Present work
$FeCr_2O_4$	Na, Mg, Fe^{2+}, Ti	Cr^{3+}, Al	BM	557.2 (4)	209 (9)	7 (1)	Fan et al. (2008)
$ZnFe_2O_4$	Zn	Fe^{3+}	BM	601.46 (5)	166 (3)	9.3 (6)	Levy et al. (2000)
$MgFe_2O_4$	Fe^{3+}	Mg	BM	591.4 (1)	182 (1)	6.3 (1)	Levy et al. (2004)
Fe_3O_4	Fe^{3+}	Fe^{2+}, Fe^{3+}	BM	591.4 (1)	182 (4)	3.6 (8)	Gotta et al. (2007)
Fe_3O_4	Fe^{3+}	Fe^{2+}, Fe^{3+}	BM	588.0 (1)	186 (5)	4.0 (fixed)	Finger et al. (1986)
Fe_2TiO_4	Fe^{2+}	Ti	BM	622 (1)	185 (20)	4.0 (fixed)	Yamanaka et al. (2009)
$MgCr_2O_4$	Mg	Cr^{3+}	HF		197.3	3.94	Catti et al. (1999)
$MnCr_2O_4$	Mn^{2+}	Cr^{3+}	HF		205.8	3.67	Catti et al. (1999)
$ZnCr_2O_4$	Zn	Cr^{3+}	HF		215.0	3.96	Catti et al. (1999)

Notes : BM and HF stand for Birch-Murnagham model and Hartree-Fock calcuration, respectively.

Table 3 Observed EoS parameters for tetrahedron and octahedron in spinels.

Spinels Chemical formual	T-site	K_0 (GPa)	M-site	K_0 (GPa)	References
$FeCr_2O_4$	Fe^{2+}	147 (9)	Cr^{3+}	275 (24)	Present work
Fe_2TiO_4	Fe^{2+}	155 (39)	Ti^{4+}	237 (19)	Yamanaka et al. (2009)
Fe_3O_4	Fe^{3+}	161 (16)	Fe^{2+}, Fe^{3+}	192 (10)	Finger et al. (1986)
Fe_3O_4	Fe^{3+}	132 (10)	Fe^{2+}, Fe^{3+}	212 (12)	Gotta et al. (2007)
$MgAl_2O_4$	Mg^{2+}	113 (15)	Al^{3+}	273 (49)	Finger et al. (1986)

Notes : Fitting the pressure-volume data to a Birch-Murnaghan EoS, a bulk modulus pressure derivative K' is fixed at 4.